

Session on Nonlinear Vibrations, Waves, and Localizations
Organized by Yusuke Doi and Masayuki Kimura

Proceedings of
the 2025 International Symposium on
Nonlinear Theory and its Applications (NOLTA2025)



Naha City, Okinawa, Japan, October 27–31, 2025.

Proceedings of NOLTA2025

© IEICE Japan2025

C3L-B Nonlinear Vibrations, Waves, and Localizations I

DATE: 2025/10/30 14:50–16:50

ROOM: Room2

C3L-B1 Moving ILMs Generated from a Static ILM in 1D and 2D FPUT–NKG Mixed Scalar Lattices

Masayuki Kimura (Setsunan University)590

C3L-B2 Coherent Interaction of Two Discrete Breathers

Sergej Flach (Institute for Basic Science)591

C3L-B3 Numerical Analysis of Band Structure of One-Dimensional Nonlinear Metamaterials Composed of Local Resonators

Kazuki Mizutani (University of Osaka), Yusuke Doi (University of Osaka), Akihiro Nakatani (University of Osaka)592

C3L-B4 Dynamic Response of Nonlinear Metamaterials with Tunable Band Gaps

Ryuki Nishio (University of Osaka), Yusuke Doi (University of Osaka), Akihiro Nakatani (University of Osaka)593

C3L-B5 Transition Waves in Origami-Based Mechanical Metamaterials

Hiromi Yasuda (Japan Aerospace Exploration Agency)597

C4L-B Nonlinear Vibrations, Waves, and Localizations II

DATE: 2025/10/30 17:00–19:00

ROOM: Room2

C4L-B1 Study on Vibration in a Lattice Free from Umklapp Processes with Strong Cubic Nonlinearity

Hiroki Ono (University of Osaka), Yusuke Doi (University of Osaka), Akihiro Nakatani (University of Osaka)684

C4L-B2 Thermal Attenuation of Soliton and Anomalous Heat Transport in the FPUT- β Lattice

Kazuyuki Yoshimura (Tottori University), Masaki Takatsu (Tottori University)687

C4L-B3 Space-Time Modulation of a Nonlinear System

Juan Archilla (Universidad de Sevilla), Masayuki Kimura (Setsunan University), Yusuke Doi (University of Osaka), Víctor Sánchez-Morcillo (Universitat Politècnica de València)691

C4L-B4 Dispersive Shock Waves from Discrete to Continuum: Some Vignettes

Panayotis Kevrekidis (University of Massachusetts Amherst)692

C4L-B5 Effect of Impurity Distribution on Propagation Speed of Nonlinear Localized Oscillation in a Mass-Spring Chain

Yosuke Watanabe (Setsunan University), Yusuke Doi (University of Osaka)693

C4L-B6 Velocity of the Traveling Intrinsic Localized Mode in the Real Self-Dual Nonlinear Network Lattice

Masayuki Sato (Kanazawa University), Yukihiro Soga (Kanazawa University)694

Moving ILMs Generated from a Static ILM in 1D and 2D FPUT–NKG Mixed Scalar Lattices

Masayuki Kimura[†]

[†]Faculty of Science and Engineering, Setsunan University
17-8 Ikeda-Nakamachi, Neyagawa, Osaka 572-8508, Japan

Email: masayuki.kimura@setsunan.ac.jp

Summary

Nonlinear coupled oscillators exhibit temporally periodic solutions with localized amplitude distributions, known as intrinsic localized modes (ILMs) or discrete breathers (DBs) [1]. Although it is well known that ILMs can move in the system without decaying their energy concentration [2], their dynamical properties are not yet well understood, especially for two- or three-dimensional systems [3, 4, 5, 6, 7]. In this study, at first, we investigated a method for generating moving ILMs by deforming the Fourier spectrum of a stationary ILM in the 1D lattices [8] which has quartic nonlinearities in both on-site and inter-site potentials, which is called Fermi–Pasta–Ulam–Tsingou–Nonlinear–Klein–Gordon (FPUT–NKG) mixed lattice. It is confirmed that the method can generate moving ILMs that move smoothly in the lattice without a decay in their energy concentration over a long period. In addition, for high-energy moving ILM, the stability change of static Sievers–Takeno mode and Page mode affects the terminal speed of the generated moving ILM. Generated moving ILMs can maintain their speed if the nonlinearity ratio in on-site and inter-site potential is close to the critical value at which the stability of static ILM changes.

Secondly, the method for generating moving ILMs from a static ILM is extended to 2D scalar square lattices. As a result, it is confirmed that moving ILMs generated by a low-energy stationary localized solution move in any direction with constant speed. In addition, properties of generated moving ILMs are investigated with respect to the amount of shift of the Fourier spectrum and the slope of the plane on which the Fourier spectrum is distributed. We found that the velocity of the moving ILMs strongly depends on the amount of shift of the Fourier spectrum, and is hardly affected by the slope of the distribution plane.


The terminal speed of generated moving ILMs is investigated with respect to the nonlinearity ratio. However, no critical values for enhancing the mobility of moving ILMs have been found. It seems to be related to the fact that the static ST mode in a 2D scalar lattice remains stable regardless of the nonlinearity ratio.

Acknowledgments

This work is supported by JSPS Kakenhi No. 24K07393 and 21K03935.

References

- [1] A.J. Sievers and S. Takeno, “Intrinsic localized modes in anharmonic crystals,” *Phys. Rev. Lett.*, vol.61, p.970, 1988.
- [2] S. Flach and A.V. Gorbach, “Discrete breathers – advances in theory and applications,” *Phys. Rep.*, vol.467, pp.1–116, 2008.
- [3] S. Aubry, “Discrete breathers: Localization and transfer of energy in discrete Hamiltonian nonlinear systems,” *Physica D*, vol.216, p.1, 2006.
- [4] K. Yoshimura and Y. Doi, “Moving discrete breathers in nonlinear lattice: Resonance and stability,” *Wave Motion*, vol.45, no.1, pp.83–99, 2007.
- [5] J.F.R. Archilla, Y. Doi, and M. Kimura, “Pterobreathers in a model for a layered crystal with realistic potentials: Exact moving breathers in a moving frame,” *Phys. Rev. E*, vol.100, p.022206, 2019.
- [6] J.B.A. Bajárs, J.C. Eilbeck, and B. Leimkuhler, “Two-dimensional mobile breather scattering in a hexagonal crystal lattice,” *Phys. Rev. E*, vol.103, p.022212, 2021.
- [7] I.A. Butt and J.A.D. Wattis, “Discrete breathers in a two-dimensional Fermi–Pasta–Ulam lattice,” *Journal of Physics A: Mathematical and General*, vol.39, no.18, p.4955, 2006.
- [8] K. Kawasaki, M. Kimura, and S. Doi, “Estimation of initial conditions for generating moving ilms from wavenumber-frequency spectrum of static ILMs in FPU–NKG mixed lattice,” 2022 International Symposium on Nonlinear Theory and Its Applications, pp.523–526, 2022.

ORCID iDs Masayuki Kimura:  0000-0002-1445-6266



This work is licensed under a Creative Commons Attribution Non Commercial, No Derivatives 4.0 License. ©IEICE 2025

Coherent interaction of two discrete breathers

Sergej Flach^{†‡}

[†]Center for Theoretical Physics of Complex Systems, Institute for Basic Science, Daejeon 34126, Republic of Korea

[‡]The New Zealand Institute for Advanced Study, Massey University Auckland, Auckland, New Zealand

Email: sergejflach@googlemail.com

Summary

I propose the possibility for two discrete breathers (also frequently called Intrinsic Localized Modes or simply ILM) to coherently exchange energy between each other.

One discrete breather (DB) is an exact solution - a time-periodic strongly localized excitation of nonlinear lattice waves [1]. Its energy dependent frequency Ω_1 is tuned out of resonance with the surrounding small amplitude lattice waves. Their dispersion ω_q forms a bounded phonon spectrum due to the underlying lattice (here q denotes a wave number/vector in reciprocal space). A DB can be approximately described as one anharmonic oscillator which in general excites all higher harmonics $k\Omega_1 \neq \omega_q$ of the fundamental DB frequency for all integer k . For lattice wave models with finite range coupling the DB localizes exponentially on the lattice with a localization length ξ_1 [2]. This length in general depends on the DB energy E_1 and its frequency Ω_1 . It tends to zero for strong frequency detuning turning the DB into an approximate single site excitation in many cases.

I argue for the possibility of a coherent interaction with a second DB with energy E_2 placed on the lattice at some distance $2d$. Both DBs form a weakly interacting nonlinear dimer. They will exchange energy with a period T_c substantially larger than their internal DB periods. T_c will grow exponentially with increasing distance $2d$. Further the DBs should exchange energy in a symmetric way, or spontaneously break parity symmetry with one DB gaining more energy than the second one, depending on their initial relative phase difference.

The above picture reminds of the beating between two oscillators. Note that two weakly interacting harmonic oscillators will exchange almost all energy with each other no matter how weak the coupling between them is. At variance, here the prediction is that the energy exchange will not be complete. That is reasonable since both DBs can be viewed as two anharmonic oscillators. Therefore their frequencies change as they start exchanging energy, tuning each other in and out of resonance.

Each DB can be approximated by one anharmonic oscilla-

Numerical Analysis of Band Structure of One-Dimensional Nonlinear Metamaterials Composed of Local Resonators

Kazuki Mizutani, Yusuke Doi, and Akihiro Nakatani

Division of Mechanical Engineering, Graduate School of Engineering, The University of Osaka
2-1, Yamadaoka, Suita-city, Osaka 565-0871, Japan,

Email: r_nishio@mech.eng.osaka-u.ac.jp, doi@mech.eng.osaka-u.ac.jp, nakatani@mech.eng.osaka-u.ac.jp

Abstract—In this study, we investigate the vibration characteristics of a metamaterial consisting of beams periodically connected to nonlinear springs. By couple the equations of motion of Euler beams and masses, we show that a band gap appears. Furthermore, by taking into account the influence of weak nonlinearity, we show that the position of the band gap shifts. In addition, we investigate the vibration characteristics by temporal evolution simulation.

1. Introduction

In recent years, metamaterials have attracted increasing attention due to their novel vibration properties. Acoustic metamaterials are attracting attention because they can achieve frequency ranges in which sound waves and elastic waves do not propagate. Such frequency ranges are called band gaps. Most research on local resonance-type metamaterials has focused on linear resonators, and various types of resonators have been proposed[1, 2]. However, studies on nonlinear localized resonator-type metamaterials are not as active as those on linear ones.

In this study, we investigate the changes in the dispersion relation of waves propagating through a beam when a small nonlinearity is introduced into the spring stiffness of a metamaterial consisting of periodically arranged linear resonators.

2. Model and Results

A uniform Euler beam with mass density ρ , Young's modulus E , second moment of area I , and cross-sectional area A is connected by a nonlinear spring with mass m at intervals of a . Let the deflection of the beam be $w(x, t)$. The equation of free vibration is given by

$$EI \frac{\partial^4 w(x, t)}{\partial x^4} + \rho A \frac{\partial^2 w(x, t)}{\partial t^2} \quad (1)$$

$$= f(u_n(t) - w(x, t))\delta(x - na), \quad (2)$$

where $\delta(x)$ is Dirac delta function, $u_n(x)$ is the displacement of n -th mass, $f(x)$ describes the nonlinear restoring force as

$$f(x) = kx + Kx^3, \quad (3)$$

Therefore, the equation of motion for the mass is given by

$$m \frac{d^2 u_n(t)}{dt^2} = f(w(na, t) - u_n(t)). \quad (4)$$

In the linear case, the dispersion relation can be calculated based on Bloch's theorem. On the other hand, in the weakly nonlinear case, by considering an effective spring constant that incorporates the effect of vibration amplitude using the averaging method, it is possible to evaluate the change in angular frequency due to amplitude variation.

An example of this analysis is shown in Fig. 1. The model considered in this study has a band gap. This is because the spring connected to the beam and the mass act as a local resonator. Furthermore, it can be seen that the upper band is shifted upward due to the effect of nonlinear interaction.

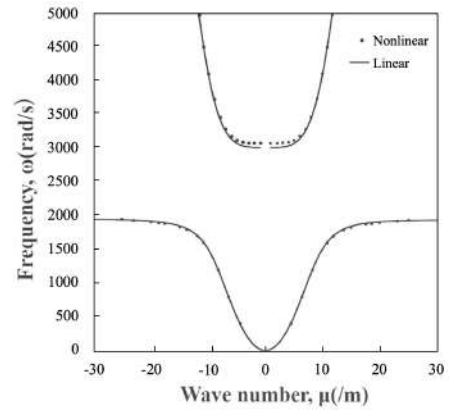


Figure 1: Dispersion relation in linear and nonlinear cases

References

- [1] Z. Liu, X. Zhang, et. al., "Locally Resonant Sonic Materials," *Science*, Vol.289, no.5485, pp.1734, 2000.
- [2] Y. Liu, D. Yu, et. al., "Design guidelines for flexural wave attenuation of slender beams with local resonators", *Physics Letters A*, Vol. 362, No. 5-6, pp. 344 – 347, 2007.

ORCID iDs Kazuki Mizutani: 0009-0003-5851-0089, Yusuke Doi: 0000-0003-3749-5353, Akihiro Nakatani: 0000-0001-7212-9303



This work is licensed under a Creative Commons Attribution Non Commercial, No Derivatives 4.0 License. ©IEICE 2025

Dynamic Response of Nonlinear Metamaterials with Tunable Band Gaps

Ryuki Nishio, Yusuke Doi, and Akihiro Nakatani

Division of Mechanical Engineering, Graduate School of Engineering, The University of Osaka
2-1, Yamadaoka, Suita-city, Osaka 565-0871, Japan,

Email: r_nishio@mech.eng.osaka-u.ac.jp, doi@mech.eng.osaka-u.ac.jp, nakatani@mech.eng.osaka-u.ac.jp

Abstract—In this paper, a metamaterial with nonlinear springs and time-delayed feedback control for broadband vibration suppression is investigated. Acoustic metamaterials possess band gaps that inhibit the propagation of waves within specific frequency ranges. We employ a mass-in-mass model equipped with time-delayed controllers and nonlinear springs to numerically investigate the influence of these components on band gap formation. The simulations demonstrate that both the time-delayed control and the nonlinear elastic elements contribute for enlargement and shift of the band gap. Furthermore, by switching the control parameters during vibration, it is possible to dynamically alter the vibrational state. These results indicate that the combination of time-delayed control and nonlinear springs enables tunable manipulation of band gap properties.

1. Introduction

Vibration and noise reduction are important engineering problems that need to be solved during design and development. Generally, metals, plastics, and glass prevent sound transmission by reflecting sound waves. Such materials suppress sound more effectively when they have heavier densities. This property is called mass law, and it is a fundamental principle of sound suppression. It means that to get a better sound insulation, we need to use heavier materials. However, it is not always possible to use heavy materials in practice, i.e., in the case of aircraft, automobiles, and other machines. To solve this problem, acoustic metamaterials is getting a lot of attention.

Metamaterials are artificially engineered periodic structures that enable the realization of unconventional physical properties not found in nature. Some metamaterials exhibit negative effective mass density[1], negative refractive index[2], and negative Poisson's ratio[3]. Acoustic metamaterials can significantly enhance sound insulation performance beyond the conventional mass law, achieving superior noise reduction while maintaining the same

weight as traditional materials. Among them, locally resonant metamaterials are classes of acoustic metamaterials that utilize the resonance of local oscillators to create band gaps. Band gaps are frequency ranges where sound waves cannot propagate[4]. The bandgap characteristics of metamaterials can be effectively exploited for vibration and noise reduction.

However, the locally resonant bandgap of these materials is relatively narrow due to the limitation of the locally resonant mechanism. Therefore, broadening and tuning the bandgap to reduce vibration and noise has become a challenge. A silicone rubber sheet made of polymer material can suppress acoustic waves in multiple frequency ranges by integrating resonators with different resonance frequencies[5, 6]. Buckling-prone elastic beams with tunable stiffness can be used to adjust acoustic bandgaps[7]. The introduction of nonlinear elements enables vibration suppression over a broad frequency range[8, 9]. Gao and Wang demonstrated that the metamaterial with optimal controller can achieve vibration suppression over the full frequency range[10].

In this paper, the vibration characteristics of a metamaterial with nonlinear springs and time-delayed feedback control are analyzed. In Section 2, a metamaterial with nonlinear springs and time-delayed control is proposed. In Section 3, the band structures and the transient response of the metamaterial are analyzed. Finally, conclusions are presented in Section 4.

2. Model and Theory

2.1. Model

This work considers a one-dimensional locally resonant metamaterial. The model is designed as shown in Fig. 1. The outer blue part is a rigid frame structure, the inner red part is a local resonator. The outer and internal masses of each unit cell are M and m , respectively. The unit cells are connected by springs with stiffness K and nonlinear springs with stiffness β . The outer and internal masses are connected by springs with stiffness k . Time-delayed controllers, “C” are applied between the outer and internal masses. The equation of motion for the n th unit cell is

ORCID iDs Ryuki Nishio:  0009-0002-4105-6038, Yusuke Doi:
 0000-0003-3749-5353, Akihiro Nakatani:  0000-0001-7212-9303



This work is licensed under a Creative Commons Attribution Non Commercial, No Derivatives 4.0 License. ©IEICE 2025

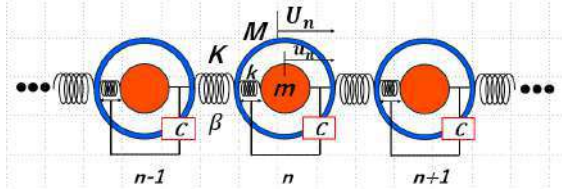


Figure 1: Model of the nonlinear metamaterial with time-delayed feedback control.

given by

$$\begin{aligned} M\ddot{U}_n + K(2U_n - U_{n+1} - U_{n-1}) + k(U_n - u_n) \\ + \beta(U_n - U_{n+1})^3 + \beta(U_n - U_{n-1})^3 - f_n = 0 \\ m\ddot{u}_n + k(u_n - U_n) + f_n = 0, \end{aligned} \quad (1)$$

where U_n and u_n are the displacements of an outer mass and an internal mass, respectively. f_n is the control force, which is given at the time instant t by

$$f_n = gk\{u_n(t - \tau) - U_n(t - \tau)\}, \quad (2)$$

where g is the dimensionless proportional gain and τ is the time delay at the time instant t .

2.2. Dispersion Relation

The harmonic wave solution of Eq. (1) takes the following complex form:

$$\begin{aligned} U_n &= Ue^{i(qna - \omega t)} \\ u_n &= ue^{i(qna - \omega t)}, \end{aligned} \quad (3)$$

where q is the wave number, a is the length of one unit cell, and ω is the angular frequency. Here, linear system is assumed to make the analysis easier. Substituting Eq. (3) into Eq. (1), we obtain

$$\begin{aligned} M\ddot{U}_n + K(2U_n - U_{n+1} - U_{n-1}) + k(U_n - u_n) \\ + gke^{i\omega\tau}(U_n - u_n) = 0 \\ m\ddot{u}_n + k(u_n - U_n) + gke^{i\omega\tau}(u_n - U_n) = 0. \end{aligned} \quad (4)$$

Using Euler's formula $e^{i\omega\tau} = \cos(\omega\tau) + i\sin(\omega\tau)$, Eq. (5) can be written as

$$\begin{aligned} M\ddot{U}_n + K(2U_n - U_{n+1} - U_{n-1}) \\ + k_{\text{eff}}(U_n - u_n) = 0 \\ m\ddot{u}_n + k_{\text{eff}}(u_n - U_n) = 0, \end{aligned} \quad (5)$$

where $k_{\text{eff}} = k + gk\cos(\omega\tau) + igk\sin(\omega\tau)$. Substituting Eq. (3) into Eq. (5), we obtain the following equations

$$\begin{bmatrix} -M\omega^2 + \alpha K + k_{\text{eff}} & -k_{\text{eff}} \\ -k_{\text{eff}} & -m\omega^2 + k_{\text{eff}} \end{bmatrix} \begin{bmatrix} U \\ u \end{bmatrix} = 0, \quad (6)$$

where $\alpha = 2 - e^{iqa} - e^{-iqa}$. This dispersion relation can be obtained as

$$\det \begin{bmatrix} -M\omega^2 + \alpha K + k_{\text{eff}} & -k_{\text{eff}} \\ -k_{\text{eff}} & -m\omega^2 + k_{\text{eff}} \end{bmatrix} = 0. \quad (7)$$

2.3. Numerical Analysis

Symplectic integrator is used to solve the equation of motion numerically. This method can conserve the Hamiltonian of the system, which is suitable for the analysis of the band gap. Equations of motion using Hamiltonian H are given by

$$\begin{aligned} \dot{q}_n &= \frac{\partial H}{\partial p_n}, \\ \dot{p}_n &= -\frac{\partial H}{\partial q_n}, \end{aligned} \quad (8)$$

where q_n and p_n are the generalized coordinates and momenta, respectively. Each coefficient of the Hamiltonian is given as, $M = 1, m = 1, K = 1, k = 2, N = 10, \delta t = 0.01$, time step = 100000. The vibration of right end cell is monitored while applying an excitation to the left end cell with $U_1 = a_0 \sin(\omega_1 t)$, where $a_0 = 0.3$ is the amplitude of the excitation and ω_1 from 0 to 10 is the angular frequency of the excitation.

3. Result and Discussion

3.1. Band Gap Formation

The band structures are shown in from Fig. 2 to Fig. 5 with or without time-delayed control, and with or without nonlinear springs. The horizontal axis is the angular frequencies, and the vertical axis is the amplitudes. Lower band (range of red line in the figures) is called acoustic mode, and upper band (range of blue line in the figures) is called optical mode[11]. The frequency range between the acoustic and optical modes is called band gap. Gray areas indicate acoustic and optical modes of linear system without time-delayed control and nonlinear springs.

By comparing Fig. 2 and Fig. 3, it can be seen that the band gap is enlarged by the time-delayed control. The band gap here is defined as the frequency range where the amplitude is less than 0.3. In Fig. 2, the band gap is from 1.05 to 2.0, while in Fig. 3, the band gap is from 0.95 to 1.93. The effect of the nonlinear springs is shown in Fig. 4, which narrows the band gap. The band gap becomes from 1.37 to 2.0, while the amplitude gets lesser for all the frequencies. In Fig. 5, the band gap is from 0.94 to 2.15, which is larger than that in Fig. 3 and Fig. 2. These results indicate that the time-delayed control and the nonlinear springs can be used to tune the band gap. The band gap can be enlarged by choosing the appropriate time-delayed control parameters while nonlinear spring stiffness can narrow the band gap.

3.2. Switching control constants

In this section, the effect of switching the control parameters is investigated. Fig. 6 shows the transient response of the right end cell with $\beta = 15, g = 0$ for $\omega_1 = 6.63$ which is a peak frequency of the band structure in Fig. 4. On the other hand, the control parameters are switched to

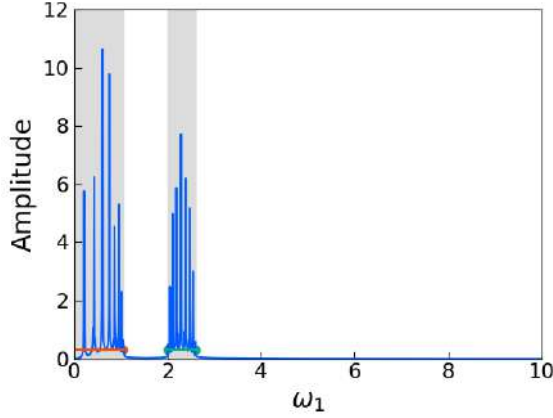


Figure 2: Band structure for (a) $\beta = 0, g = 0$.

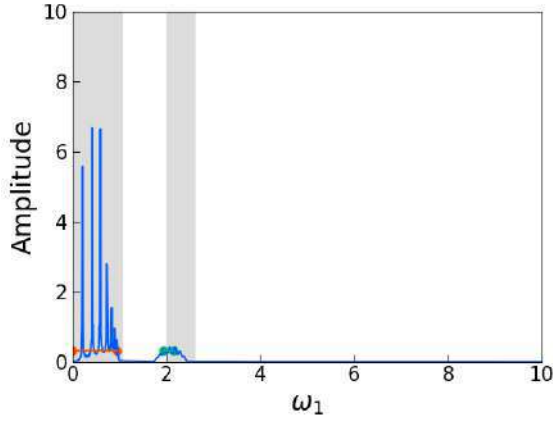


Figure 3: Band structure for (b) $\beta = 0, g = -0.25, \tau = 0.05$.

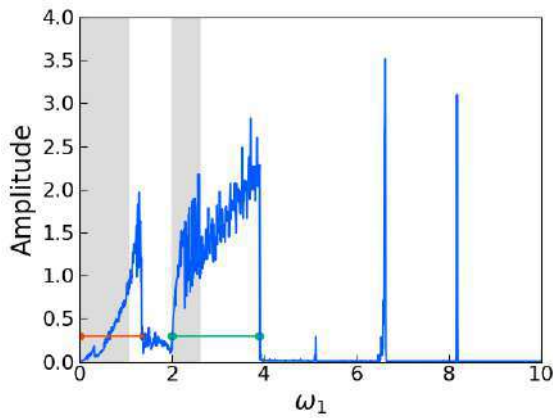


Figure 4: Band structure for (c) $\beta = 0, g = -0.25, \tau = 0.05$.

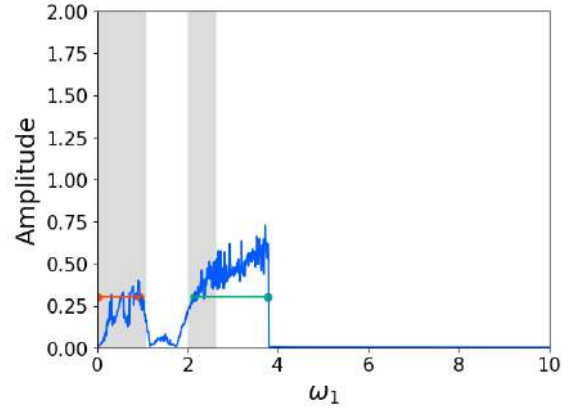


Figure 5: Band structure for (d) $\beta = 15, g = -0.25, \tau = 0.1$.

$g = -0.25, \tau = 0.05$ at $t = 500$ in Fig. 7. In Fig. 6, the amplitude of the right end cell gradually increases and reaches a peak value of around 4 at $t = 1000$. In Fig. 7, the amplitude of the right end cell is suppressed to around 0.1 after the control parameters are switched. This result indicates that swiyching the control parameters can effectively suppress the vibration of the metamaterial.

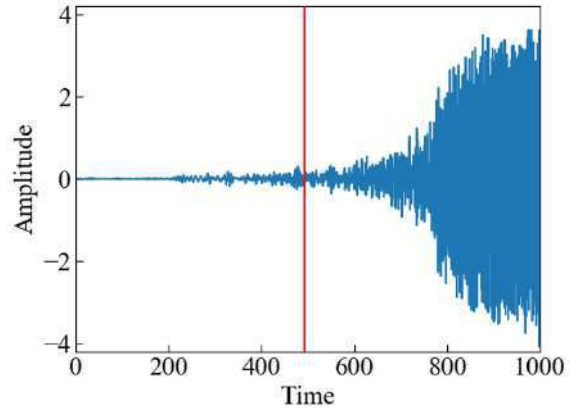


Figure 6: Transient response of the right end cell for $\omega_1 = 6.63$ with $\beta = 15, g = 0$.

4. Conclusion

In this paper, a metamaterial with nonlinear springs and time-delayed feedback control is proposed, and broadband vibration suppression is investigated. Both the time-delayed feedback control and the nonlinear elastic elements contribute to the enlarge or shift the band gap. Furthermore, by switching the control parameters during vibration, it is possible to dynamically alter the vibrational state. These results indicate that the combination of time-delay control and nonlinearity enables tunable manipulation of band gap properties.

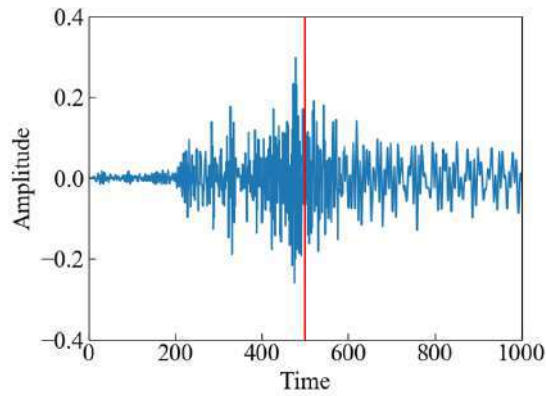


Figure 7: Transient response of the right end cell for $\omega_1 = 6.63$ when control parameters change from $\beta = 15, g = 0$ in $0 \leq t \leq 500$ to $\beta = 15, g = -0.25, \tau = 0.05$ in $500 \leq t \leq 1000$.

References

- [1] H. H. Huang and C. T. Sun, "Wave attenuation mechanism in an acoustic metamaterial with negative effective mass density", *New Journal of Physics*, vol.11, 013003, 2009.
- [2] S. A. Cummer, J. Christensen and A. Alu, "Controlling sound with acoustic metamaterials," *Nature Reviews Materials*, vol.1, no. 16001, 2016.
- [3] K. E. Evans and A. Alderson, "Auxetic Materials: Functional Materials and Structures from Lateral Thinking!," *Advanced Metamaterials*, vol.12, no.9, pp.617-681, 2000.
- [4] Z. Liu, X. Zhang, et al., "Locally Resonant Sonic Materials," *Science*, Vol.289, no.5485, pp.1734, 2000.
- [5] L. Sanguilano, B. Reff, et al., "Low frequency tyre noise mitigation in a vehicle using metal 3D printed resonant metamaterials," *Mechanical Systems and Signal Processing*, Vol.179, 109335, 2022.
- [6] M. Nakayama, T. Matsuoka, et al., "A practically designed acoustic metamaterial sheet with two-dimensional connection of local resonators for sound insulation applications," *Journal of Applied Physics*, vol.129, no.10, 2021.
- [7] P. Wang, F. Casadei, et al., "Harnessing Buckling to Design Tunable Locally Resonant Acoustic Metamaterials," *Physical Review Letters*, vol.113, 014301, 2014.
- [8] X. Fang, J. Wen, et al., "Ultra-low and ultra-broadband nonlinear acoustic metamaterials," *Nature Communications*, vol 8, no.1288, 2017.
- [9] X. Fang, J. Wen, et al., "Broadband and tunable one-dimensional strongly nonlinear acoustic metamaterials: Theoretical study," *Physical Review E*, vol.94, 052206, 2016.
- [10] Y. Gao, L. Wang, "Broad bandgap active metamaterials with optimal time-delayed control," *International Journal of Mechanical Sciences*, vol.254, 108449, 2023.
- [11] A. V. Porubov, A. M. Krivtsov, "Dispersive propagation of localized waves in a mass-in-mass metamaterial lattice," *Continuum Mechanics and Thermodynamics*, vol.34, pp.1475, 2022. *Physical Review Letters*, vol.89, 134102, 2002.

Transition waves in origami-based mechanical metamaterials

Hiromi Yasuda[†]

[†]Department of Space Flight Systems, Institute of Space and Astronautical Science,
Japan Aerospace Exploration Agency
3-1-1 Yoshinodai, Chuo-ku, Sagami-hara, Kanagawa 252-5210, Japan,

Email: yasuda.hiromi@jaxa.jp

Abstract– We study nonlinear wave dynamics in origami-based mechanical metamaterials, specifically the propagation of transition waves. Our origami structure can be multistable depending on the chosen geometric parameters. We numerically analyze the tailorable behavior of our origami units by introducing a simplified model. Also, we fabricate prototypes and validate such tailorable multistable behavior based on quasi-static force-displacement measurements. Then, we examine wave propagation in a 1D chain of origami units. By applying the input only to the end of the chain, we experimentally demonstrate the phase change of each origami unit and the formation of the phase boundary moving from one end to the other, i.e., transition waves. Since a simple actuation can trigger the reconfiguration of the entire system, our origami-based mechanical metamaterials have great potential for designing a new engineering device, especially for space applications.

Study on Vibration in a Lattice Free from Umklapp Processes with Strong Cubic Nonlinearity

Hiroki Ono[†], Yusuke Doi[†], and Akihiro Nakatani[†]

[†]Division of Mechanical Engineering, Graduate School of Engineering, The University of Osaka
2-1 Yamadaoka, Suita, Osaka, 565-0871, Japan,

Email: ono@md.mech.eng.osaka-u.ac.jp, doi@mech.eng.osaka-u.ac.jp, nakatani@mech.eng.osaka-u.ac.jp

Abstract—We study on vibration for the lattice with cubic nonlinearity. The lattice is called umklapp free lattice (UFL) for its property that no umklapp processes occurs. In the previous work, it was shown that the size dependence of the thermal conductivity in that UFL increases as the cubic nonlinearity becomes stronger. On the other hand, the mechanism is not unclear that the reduction of the thermal conductivity is observed in the regime of strong cubic nonlinearity of the UFL. In this study, we focus on phonon group velocity and describe dispersion relations of the UFL. As a result of numerical simulation, it is shown that group velocity becomes slow as the cubic nonlinearity becomes stronger. In addition, dispersion relations are derived theoretically.

1. Introduction

Non-Fourier thermal transport is observed numerically [1, 2, 3, 4] and experimentally [5] in nano-scale. Thermal transport in nano-scale can be classified by considering size dependence of the thermal conductivity. Especially, the ballistic thermal transport is known as the form that heat fluxes does not decay with increasing of the size of system. Conserved quantity plays an important role in realizing the ballistic thermal transport. Integrable systems, such as Toda lattice [6], have conserved quantity corresponding to degree of freedom, and the ballistic thermal transport can be observed. It is shown that umklapp processes, which occurred by phonon interactions, disturb the ballistic thermal transport [7]. Yosimura *et al.* constructed the umklapp free lattice (UFL), and verified the Peierls's hypothesis [8]: the thermal resistance is caused by only umklapp processes.

Phonon dispersion relation gives us the characteristics of thermal transport from the point of view of phonons. In the linear system, the dispersion relation can be obtained strictly. Special structure of dispersion relations can be obtained such as flat band [11] depending on the structure of linear lattices. On the other hand, in nonlinear systems, it is difficult to describe dispersion relations explicitly. One of

the difficulties comes from phonon interactions. Phonons excite other ones due to nonlinearity, and the mechanism of phonon excitation becomes complex as the system becomes thermalization [9]. The UFL overcomes this difficulty only in the regime of wave number of phonons such that umklapp processes do not occur [7].

In this study, we focus on the UFL in the regime of strong cubic nonlinearity compared with quartic nonlinearity. The non-equilibrium steady state simulation is performed to investigate thermal transport and the dispersion relation in the UFL. Vibrational analysis is also done to derive the dispersion relation theoretically.

2. Lattice model and numerical simulations




Let introduce the 1D cubic nonlinear lattice described by Hamiltonian

$$H = \sum_{n=1}^N \frac{1}{2} p_n^2 + \sum_{n=1}^N \frac{1}{2} (q_{n+1} - q_n)^2 + \frac{\alpha}{3} \sum_{n=1}^N \sum_{r=1}^R a_r [q_{n+r} - (-1)^r q_n]^3 + \frac{\beta}{4} \sum_{n=1}^N \sum_{r=1}^R b_r [q_{n+r} - (-1)^r q_n]^4, \quad (1)$$

where q_n, p_n , $n = 1, 2, \dots, N$ are n -th displacement from equilibrium point and momentum, respectively. N is the number of particle, α, β are the factor of the cubic and quartic nonlinear potential, respectively, and $a_r = [1 - (-1)^r] / 2r^2$, $b_r = 1/r^2$. R is the cutoff coefficient of long-range nonlinearity. Explicit representation of factors a_r and b_r are obtained in studies by considering the invariance of Hamiltonian (1) for the special map [10].

Numerical simulations are performed to investigate the thermal conductivities and phonon dispersion relations of the proposed UFL (1). Figure 1 shows the illustration of the numerical simulation. The UFL is connected with two Langevin thermostats via only linear interactions. Fixed boundary conditions are applied to the end of thermostats.

The thermal conductivity is calculated as follows: Two

ORCID iDs Hiroki Ono:  0009-0009-2573-3140, Yusuke Doi:  0000-0003-3749-5353, Akihiro Nakatani:  0000-0001-7212-9303



This work is licensed under a Creative Commons Attribution Non Commercial, No Derivatives 4.0 License. ©IEICE 2025

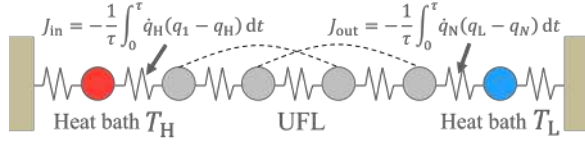


Figure 1: Illustration of numerical simulation model. Langevin thermostats are connected with the UFL at both ends.

heat fluxes J_{in}, J_{out} are defined as

$$J_{in} = -\frac{1}{\tau} \int_0^\tau \dot{q}_H (q_1 - q_H) dt, \quad (2)$$

$$J_{out} = -\frac{1}{\tau} \int_0^\tau \dot{q}_N (q_L - q_N) dt, \quad (3)$$

where q_H and q_L are displacement of particles in thermostats with T_H and T_L connected with the UFL, respectively. q_1 and q_N are also displacement of particle in the UFL located in the end of left right side, respectively. J_{in} is the inflow from the thermostat with temperature T_H , and J_{out} is the outflow for the thermostat with temperature T_L . We denote the thermal conductivity κ by using J_{in}, J_{out} as

$$\kappa = \frac{J_{in} + J_{out}}{T_H - T_L} N. \quad (4)$$

The following relation is used to classify change of κ with increasing N :

$$\kappa \propto N^c, \quad 0 \leq c. \quad (5)$$

The thermal conductivity κ is computed for different $N = 200, 400, 1000, 2000, 4000, 10000, 20000, 40000, 100000$. Parameters are as follows: $R = 200, T_H = 1.2, T_L = 0.8, (\alpha, \beta) = (0.01, 0.01), (0.1, 0.1)$. The velocity Verlet scheme is applied to solve equation of motions obtained from Eq. (1). The time step Δt is 0.01. After first 1.5×10^7 steps are passed, we assume that the system reaches non-equilibrium steady states. κ is computed each 20 steps and its average is used as the effective thermal conductivity.

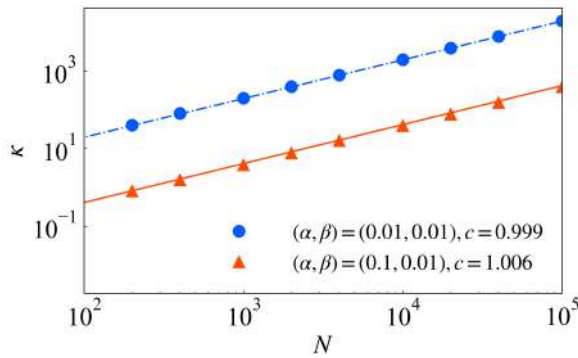


Figure 2: The change of thermal conductivities κ in the UFL vs the system size N .

The change of thermal conductivities is indicated in Fig. 2. Figure. 2 shows two sets of numerical results, corresponding to different factors $(\alpha, \beta) = (0.01, 0.01), (0.1, 0.01)$. First, consider the weak cubic nonlinear case $(\alpha, \beta) = (0.01, 0.01)$, which is shown by blue circles. We obtain relation $\kappa \propto N^{0.999}$, and thermal transport remains ballistic. The mechanism of ballistic thermal transport is expected as follows: this is the regime of weak nonlinearity; therefore the linear interaction mainly contributes to ballistic thermal transport. Next, we focus on the strong cubic nonlinear case $(\alpha, \beta) = (0.1, 0.01)$, which is shown by orange triangles. Ballistic thermal transport is also observed ($\kappa \propto N^{1.006}$) despite the strong cubic nonlinearity. This shows that the concept of umklapp free in the UFL is independent from the strength of nonlinearity. On the other hand, κ is 10 times smaller than that of the weak cubic nonlinear case. This change implies that the group velocity of phonons drastically decreases as the strength of cubic nonlinearity increases.

It is worth describing the dispersion relation to investigate the nature of phonons in the UFL. The scheme used to compute the thermal conductivity is applied and N is fixed at $N = 16384$. Time series data of q_n are recorded for 3.0×10^5 steps, and the dispersion relation is obtained by fast Fourier transform.

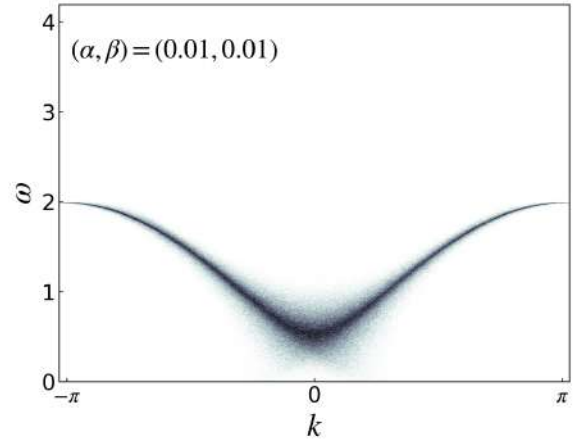


Figure 3: The dispersion relation for the case $(\alpha, \beta) = (0.01, 0.01)$.

Two dispersion relations are shown in Fig. 3 and Fig. 4. Horizontal lines are wave number k , and vertical lines are frequency of phonons ω . It is revealed that the group velocity of phonons, which is defined as $\partial\omega/\partial k$, becomes small as the strength of cubic nonlinearity increases. Bandwidth is also affected by the cubic nonlinearity, and the dispersion relation becomes flat band [11] like in the regime of strong cubic nonlinearity. It should be stressed that this reduction of bandwidth can be observed by changing factors corresponding to the nonlinearity; it is independent from linearity.

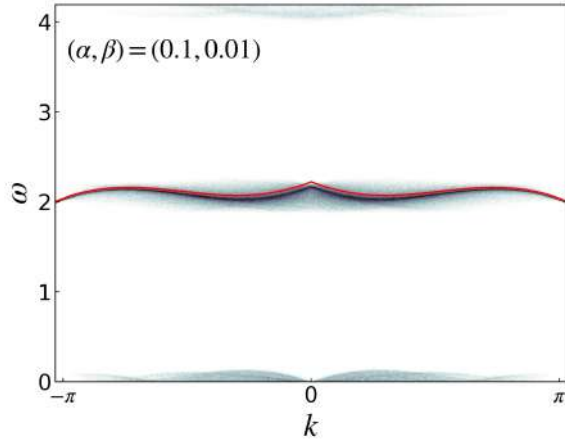


Figure 4: The dispersion relation for the case $(\alpha, \beta) = (0.1, 0.01)$. The red line is derived analytically (13).

3. Analytic derivation of dispersion relations

In this section, dispersion relations are obtained analytically. Applying periodic boundary condition to the UFL (1) and considering the limit $N \rightarrow \infty$, following equation of motion is obtained:

$$\begin{aligned} \ddot{q}_n = & q_{n+1} - 2q_n + q_{n-1} \\ & - \alpha \sum_{r=1}^{\infty} a_r (-1)^r [q_{n+r} - (-1)^r q_n]^2 \\ & + \alpha \sum_{r=1}^{\infty} a_r [q_n - (-1)^r q_{n-r}]^2 \\ & - \beta \sum_{r=1}^{\infty} b_r (-1)^r [q_{n+r} - (-1)^r q_n]^3 \\ & + \beta \sum_{r=1}^{\infty} b_r [q_n - (-1)^r q_{n-r}]^3. \end{aligned} \quad (6)$$

We assume the single mode solution as

$$q_n(k, t) = U_k(t)e^{ikn} + U_{-k}(t)e^{-ikn} + U(t), \quad (7)$$

where U_k, U_{-k}, U are complex normal coordinates. k is restricted to its range as $k \in (\pi/2, \pi]$. $U(t)$ is necessary by following reason: let introduce the new variables q_G as

$$q_G = \sum_{n=1}^{\infty} q_n, \quad (8)$$

and consider the equation of motions of q_G :

$$\begin{aligned} \ddot{q}_G = & -\alpha \sum_{n=1}^{\infty} \sum_{r=1}^{\infty} \frac{1}{(2r-1)^2} (q_{n+2r-1} + q_n)^2 \\ & - \beta \sum_{n=1}^{\infty} \sum_{r=1}^{\infty} \frac{1}{(2r-1)^2} (q_{n+2r-1} + q_n)^3. \end{aligned} \quad (9)$$

The right-hand side (RHS) in Eq. (9) becomes zero when $q_n \equiv 0$ or $-\alpha/2\beta$. Both of them is equilibrium points, and the latter is generated by considering the cubic nonlinearity. Moreover, if the cubic nonlinearity is included, only the latter is stable point. Therefore, $U(t)$ is necessary to consider dispersion relation at the neighbor of stable point in the UFL with cubic nonlinearity.

Substituting Eq. (7) into Eq. (6), these are reduced as

$$\begin{aligned} \ddot{U}_k = & -\omega_k^2 U_k \\ & -6\beta_k U_k^2 U_{-k} + 6\beta_k U^2 U_k + 2\alpha_k U U_k, \end{aligned} \quad (10)$$

$$\begin{aligned} \ddot{U} = & -2\alpha_k U_k U_{-k} - 12\beta_k U U_k U_{-k} \\ & -\alpha\pi^2 U^2 - 2\beta\pi^2 U^3, \end{aligned} \quad (11)$$

where $\alpha_k = \alpha(\pi - k), \beta_k = \beta(\pi - k)$.

In the following discussion, three regimes of cubic nonlinearity are considered: (i) $\alpha \gg \beta$ (strong cubic nonlinearity), (ii) $\alpha \ll \beta$ (weak cubic nonlinearity), (iii) $\alpha = 0$ (Only quartic nonlinearity). Assuming that the solution of Eqs. (10), (11) is traveling wave, the relation between ω and k is obtained as dispersion relations.

3.1. The case of $\alpha \gg \beta$

Assuming that

$$U_k(t) = \frac{A}{2} \frac{\alpha}{2\beta} e^{-i\omega t}, U(t) = -\frac{\alpha}{2\beta}, \quad (12)$$

as the traveling wave, where A is the amplitude of traveling wave, then the dispersion relation

$$\omega(k) = \sqrt{\omega_k^2 + \frac{\alpha}{\beta} \alpha_k \pi \left(\frac{1}{2} + \frac{3}{8} A^2 \right)} \quad (13)$$

is obtained, where $\omega_k = 2 \sin k/2$. The red line shown in Fig. 4 corresponds to the curve defined by Eq. (13). It is shown that Eq. (13) is in good agreement with the dispersion relation described by the numerical simulation. In the case that A is much smaller than α/β , such as the regime of low temperature, the term $3/8 A^2$ can be neglected and the dispersion relation depends on the parameter α^2/β .

3.2. The case of $\alpha \ll \beta$

Assuming that

$$U_k(t) = \frac{A}{2} e^{-i\omega t}, U(t) \equiv 0, \quad (14)$$

as the traveling wave, the dispersion relation

$$\omega(k) = \sqrt{\omega_k^2 + \frac{3}{2} A^2 \pi (\pi - k) + \frac{\alpha^2}{\beta}} \quad (15)$$

is obtained. Compared with Eq. (13), contribution of cubic nonlinearity appears as the term α^2/β .

3.3. The case of $\alpha = 0$

If cubic nonlinearity disappears, we only consider Eq. (10). Substituting $\alpha = 0$ into Eq. (10), the following equation is obtained:

$$\ddot{U}_k = -\omega_k^2 U_k - 6\beta_k (U_k^2 U_{-k} + U^2 U_k). \quad (16)$$

Assuming that

$$U_k(t) = \frac{A}{2} e^{-i\omega t} \quad (17)$$

as the traveling wave, we have

$$\omega(k) = \sqrt{\omega_k^2 + \frac{3}{2} A^2 \pi(\pi - k)} \quad (18)$$

as the dispersion relation.

4. Conclusion

In this study, thermal transport and dispersion relations in the UFL with strong cubic nonlinearity are analyzed. The non-equilibrium steady state simulation is performed to investigate the thermal conductivity in the UFL. It is shown that thermal transport is invariant for the change of strength of cubic nonlinearity, while the thermal conductivity is affected by it. Phonon dispersion relations are described numerically and theoretically to focus on propagation of phonon. It is revealed that group velocity of phonons decreases as the strength of cubic nonlinearity increases. Bandwidth is also affected by the change of cubic nonlinearity, and the UFL becomes flat band like system in the regime of strong cubic nonlinearity.

References

- [1] J. Shiomi and S. Maruyama, Non-fourier heat conduction in a single-walled carbon nanotube: Classical molecular dynamics simulations, *Phys. Rev. B*, 73:205420, 2006.
- [2] G. Benenti, D. Donadio, S. Lepri, and R. Livi, Non-fourier heat transport in nanosystems, *La Rivista del Nuovo Cimento*, 46, 2023.
- [3] F. Andreucci, S. Lepri, S. Ruffo, and A. Trombettoni, Nonequilibrium steady states of long-range coupled harmonic chains, *Phys. Rev. E*, 108(2):024115, 2023.
- [4] M. Takatsu, T. Kitamura, and K. Yoshimura, A large scale non-equilibrium simulation of heat transport in one-dimensional fermi–pasta–ulam–tsingou lattice, *Journal of the Physical Society of Japan*, 93(5):053001, 2024.
- [5] C. W. Chang, D. Okawa, H. Garcia, A. Majumdar, and A. Zettl, Breakdown of fourier’s law in nanotube thermal conductors, *Phys. Rev. Lett.*, 101(7):075903, 2008.
- [6] M. Toda, Vibration of a chain with nonlinear interaction, *Journal of the Physical Society of Japan*, 22(2):431–436, 1967.
- [7] K. Yoshimura, Y. Doi, and T. Kitamura, Heat transport in nonlinear lattices free from the umklapp process, *Phys. Rev. E*, 105(2):024140, 2022.
- [8] R. Peierls. On the kinetic theory of thermal conduction in crystals, In R. H. Dalitz and Sir Rudolf Peierls, editors, *Selected Scientific Papers of Sir Rudolf Peierls*, pages 15–48. World Scientific, 1997.
- [9] Y. Guo, Y. Sun, and L. Wang, Thermalization process in a one-dimensional lattice with two-dimensional motions: The role of angular momentum conservation, *Phys. Rev. E*, 108:014127, 2023.
- [10] K. Yoshimura, G. Kato, and Y. Doi, A symmetry of potential function and non-relaxation theorems of heat flux in nonlinear lattice, *Physica D: Nonlinear Phenomena*, 446:133638, 2023.
- [11] D. Leykam, A. Andreanov, and S. Flach, Artificial flat band systems: from lattice models to experiments, *Advances in Physics: X*, 3(1):1473052, 2018.

Thermal attenuation of soliton and anomalous heat transport in the FPUT- β lattice

Kazuyuki Yoshimura[†] and Masaki Takatsu[‡]

[†]Faculty of Engineering, Tottori University, 4-101 Koyama-Minami, Tottori 680-8552, Japan,

[‡]Graduate School of Sustainability Science, Tottori University, 4-101 Koyama-Minami, Tottori 680-8552, Japan

Email: kazuyuki@tottori-u.ac.jp

Abstract—The energy attenuation process of a soliton propagating through a thermally excited interval of the one-dimensional Fermi-Pasta-Ulam-Tsingou β lattice is investigated. We show the power law $\Delta E/E_{in} \propto E_{in}^c$, where E_{in} is the initial soliton energy and ΔE is the amount of average energy decrease after propagating the interval. The exponent is obtained as $c \simeq 1.65$, which is close to $5/3$. Based on this power law, we develop a theory which describes the energy of attenuating soliton as a function of the propagation length, and it well agrees with numerical results. Moreover, assuming energy transport by the attenuating solitons, we derive the power law $\kappa \propto N^\alpha$ which characterizes the anomalous heat transport, where κ is the thermal conductivity, N is the lattice size, and $\alpha = 1 - c^{-1} \simeq 0.394$. This value of α is close to $2/5$ and coincides with that of direct nonequilibrium simulation. The energy transport by attenuating solitons is a possible mechanism of the anomalous heat transport.

1. Introduction

Heat transport in macroscopic scale materials is well described by the Fourier's law $J = -\kappa \nabla T$, where J and ∇T are the heat flux and the temperature gradient, respectively, and κ is a material constant called the thermal conductivity. This is called the *normal* heat transport. On the other hand, the Fourier law does not always hold in microscopic scale materials of near one-dimensional shapes. Non-Fourier or *anomalous* heat transport, in which κ is not a constant but increases with the object length, has been experimentally observed in carbon and boron-nitride nanotubes [1].

A simple dynamical model for studying heat transport in microscopic scale is one-dimensional nonlinear lattice. A number of studies using this model have revealed that the thermal conductivity κ in general follows the power law $\kappa \propto N^\alpha$, $0 \leq \alpha \leq 1$ for the lattice size N . The normal heat transport of $\alpha = 0$ is observed in several lattice models [2, 3, 4]. On the other hand, it has been found that some lattices exhibit $\alpha > 0$, i.e., κ diverges as N increases. An

extreme case is the *ballistic* transport of $\alpha = 1$, which implies that the thermal resistance completely disappears, and it is observed only in lattices having special properties such as the Toda lattice [5] and the umklapp-free lattice [6]. The generic anomalous transport is the case of $0 < \alpha < 1$, and it has been numerically observed in nonlinear lattices that conserve total momentum such as the Fermi-Pasta-Ulam-Tsingou β (FPUT- β) [7, 8, 9, 10], FPUT- α [11], and diatomic Toda [12] lattices. The exponent α commonly takes values of around 0.3 to 0.4. This fact suggests a common mechanism behind the anomalous heat transport, but it has not yet been clarified.

In order to clarify the mechanism, it is essential to properly understand the propagation process of a wave which dominantly carries thermal energy. In this study, we deal with the FPUT- β lattice. Although a definitive conclusion is not settled in, effective phonon [13] or soliton [14] has been considered to be the thermal energy carrying wave. Here, focusing on the soliton, we numerically investigate the energy attenuation of solitons propagating in the FPUT- β lattice with a non-zero temperature and show that a power law holds for the average energy attenuation rate. Moreover, we develop a theory of energy transport by the attenuating solitons, based on this power law. This theory leads to the power law $\kappa \propto N^\alpha$ and gives the value of α in good agreement with that obtained by a nonequilibrium simulation [10]. This agreement suggests that the energy transport by attenuating soliton is a possible mechanism of the anomalous heat transport.


2. FPUT- β lattice and soliton

The one-dimensional FPUT- β lattice is a chain of unit-mass particles and described by the Hamiltonian

$$H = \sum_n \frac{1}{2} p_n^2 + \sum_n \left[\frac{1}{2} (q_{n+1} - q_n)^2 + \frac{\beta}{4} (q_{n+1} - q_n)^4 \right], \quad (1)$$

where q_n and p_n represent the displacement and momentum of n th particle, respectively, and β is the nonlinearity strength parameter. We fix $\beta = 1$ in this study. The equations of motion read

$$\ddot{q}_n = q_{n+1} - 2q_n + q_{n-1} + \beta \left[(q_{n+1} - q_n)^3 - (q_n - q_{n-1})^3 \right]. \quad (2)$$

ORCID iDs Kazuyuki Yoshimura:  0000-0002-4329-4999



This work is licensed under a Creative Commons Attribution Non Commercial, No Derivatives 4.0 License. ©IEICE 2025

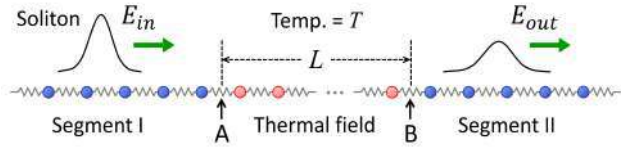


Figure 1: Illustration of numerical experiment setup.

It is well known that the FPUT- β lattice has soliton solutions. An approximate soliton can be obtained via continuum approximation as follows:

$$q_n = \frac{1}{\sqrt{6\beta}} \tan^{-1} \left(\sinh \sqrt{6\beta A} (n - ct - x_0) \right) - \frac{\pi}{2\sqrt{6\beta}}, \quad (3)$$

where x_0 is a constant representing the soliton center at $t = 0$, c and A are the velocity and amplitude of soliton, respectively, and they relate with each other via $c^2 = 1 + \beta A/2$. The sound speed is unity, and the soliton is supersonic as $c > 1$. The second term in Eq. (3) was chosen so that $q_n \rightarrow 0$ may hold in the limit $n \rightarrow +\infty$. If we numerically integrate Eq. (2) with the initial condition $q_n(0)$ and $\dot{q}_n(0)$ obtained from Eq. (3), then there appear a soliton and small ripples. This soliton eventually ceases radiating ripples after it propagates over a long distance. This radiation-less soliton is regarded as a numerically exact soliton and will be used in our numerical experiments. We will use only a rarefaction soliton. This is enough because time evolution in the case of compression soliton is obtained by just reversing the sign of q_n in that of rarefaction one due to the even symmetry of the FPUT- β interaction potential.

3. Setup of numerical experiments

We investigate the propagation process of a soliton in a thermalized interval of the FPUT- β lattice, in which the soliton exchanges its energy with thermally excited phonons and in average loses its energy. We call this interval the *thermal field*. Figure 1 illustrates the setup of our numerical experiments. The FPUT- β lattice of a large enough size is used, which has the open and fixed-end boundary conditions at the left and right ends, respectively. Let L be the length of the thermal field and T be its temperature. The particles inside the thermal field are indexed with $n \in I := \{n_0 + 1, \dots, n_0 + L\}$.

Our numerical experiments were carried out by the following steps.

1. A thermal equilibrium state of the thermal field is generated by equipping the Langevin heat bath at temperature T to the particles of $n \in I$. Then, the Langevin heat bath is turned off. In this process, the couplings at both ends of the thermal field indicated by arrows

A and B are disconnected so that the energy may not flow outward.

2. A numerically exact soliton is put in the segment I, and then it propagates from left to right. The soliton's initial energy E_{in} is measured.
3. The coupling of arrow A is connected just before the soliton reaches the thermal field. The soliton enters into and propagates through the thermal field.
4. The coupling of arrow B is connected just before the soliton reaches the right end of the thermal field to let the soliton go out.
5. The soliton propagates in the segment II. It is accompanied by phonons in the early stage, but the soliton and the phonons eventually separate with each other since the soliton is supersonic. After separation, the transmitted soliton's energy E_{out} is measured.

We describe the procedure for measuring the energy of soliton in the steps 2 and 5. Let J_n be the energy flow between n th and $(n+1)$ th particles per a unit time. It is given by

$$J_n = \dot{q}_{n+1} \cdot F(q_{n+1} - q_n), \quad F(r) = -r - \beta r^3. \quad (4)$$

Choose a particle in the segment I, and let n_1 be its index. A soliton passes this position in the step 2. The initial energy E_{in} of this soliton can be obtained by the integral

$$E_{in} = \int_{t_s}^{t_e} J_{n_1}(t) dt, \quad (5)$$

where t_s and t_e are the times at which the soliton's front and end pass the position n_1 , respectively. The front and end are approximately determined by a cutoff. The transmitted soliton's energy E_{out} is obtained in a similar manner just by appropriately choosing n_2 in the segment II instead of n_1 .

In our numerical experiments, we repeat the steps 1 to 5 for many times over different realizations of the thermal field, once T , L , and E_{in} are fixed. The energy E_{out} is different for each sample. In an average, the energy of soliton decreases after propagating over the thermal field, while in each trial the energy can either increase or decrease. We define the energy attenuation rate R of soliton by

$$R = \frac{E_{in} - \langle E_{out} \rangle}{E_{in}}, \quad (6)$$

where $\langle E_{out} \rangle$ represents the average of E_{out} over realizations of the thermal field.

4. Results of numerical experiments

Figure 2 shows the attenuation rate R as a function of initial soliton energy E_{in} in log-log scale for three different lengths of the thermal field $L = 500, 1000$, and 2000 , where

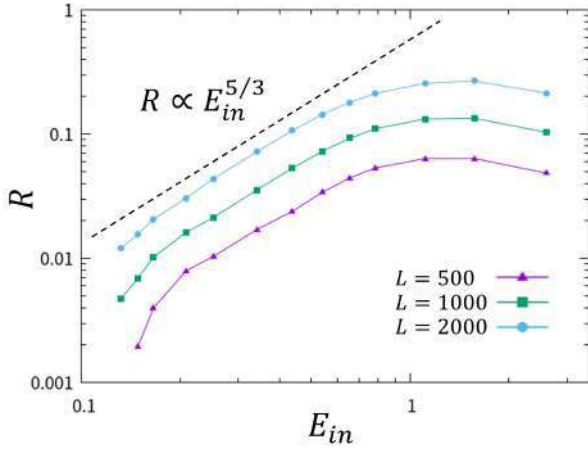


Figure 2: Attenuation rate R as a function of soliton energy E_{in} for different lengths $L = 500, 1000$, and 2000 , where $T = 0.02$. Dashed line represents the power law $R \propto E_{in}^{5/3}$.

the temperature is fixed as $T = 0.02$. We used 10^4 samples to obtain each data point in Fig. 2.

It is clearly observed that the data points lie on a straight line in a region of small E_{in} , approximately $E_{in} < 0.5$, for each L . Moreover, such lines have almost the same slope for three values of L . This fact implies the power law

$$R \propto E_{in}^c, \quad (7)$$

where c is a constant independent of L . We performed a least-square fitting of the function $R = a_L E_{in}^c$ to six data points for $L = 2000$ which are in the range $0.16 < E_{in} < 0.6$, where a_L and c are the fitting parameters and the prefactor a_L depends on the choice of L . It gives $c \approx 1.65$, which is close to $5/3$, and $a_L \approx 0.42$. A reference line of the power law $R \propto E_{in}^{5/3}$ is shown by dashed line. The slope of this reference line well coincides with that of the data points for each L value, confirming the power law Eq. (7) and that c is independent of L .

In a region of very small E_{in} , some deviation from the power law is seen for any of the L values. It may be due to a finite length effect of the thermal field. Indeed, the deviation becomes smaller with increasing L .

5. Soliton propagation theory

We develop a theory for describing the mean energy $E(x)$ of soliton as a function of its propagation length x based on Eq. (7), where x is considered as a continuous variable. If we apply the power law to the interval between x and $x + L$ and make some calculation, we have

$$\frac{E(x+L) - E(x)}{L} = -\frac{a_L}{L} E^{c+1}(x), \quad (8)$$

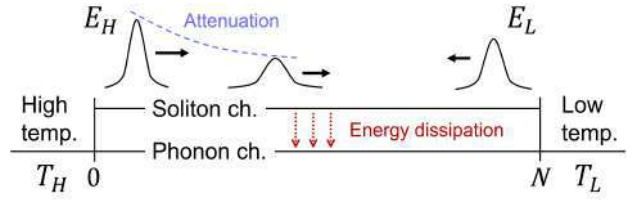


Figure 3: Schematic illustration of heat transport by attenuating solitons and phonons.

where a_L is the prefactor in the power law. Since the left hand side can be approximated by the derivative dE/dx , we can obtain the differential equation

$$\frac{dE}{dx} = -aE^{c+1}, \quad (9)$$

where $a = a_L/L$ and it is independent of L . This equation is easily solved, and its solution is obtained as follows:

$$E(x) = (acx + b)^{-1/c}, \quad (10)$$

where b is an integration constant and it relates with $E(0)$ via $b = (1/E(0))^c$. This solution gives $E(x) \propto x^{-1/c}$ for large x . We have confirmed a good agreement between the numerical results and $E(L)$ obtained from Eq. (10). That is, equation (10) can well describe the energy attenuation of soliton.

6. A theory for anomalous heat transport

We develop a simple theory for explaining the mechanism of anomalous heat transport. Our theory assumes that thermal energy is transported via two types of channels: one is the channel of attenuating solitons and the other is that of phonons. In addition, the phonon channel is assumed to exhibit the normal heat transport. Consider a lattice of size N in the state of steady heat transport caused by two heat baths with high and low temperatures T_H and T_L . We suppose that solitons are generated at the high temperature side and propagate to the low temperature side, attenuating their energy. The energy lost from the solitons may flow into the phonon channel. The same process is supposed to occur in solitons propagating in the opposite direction. Figure 3 illustrates this scenario.

We calculate the thermal conductivity κ as a function of N based on the scenario in Fig. 3 and show that it well explains the scaling law $\kappa \propto N^{0.394}$ which has been obtained by a direct nonequilibrium simulation in Ref. [10]. Assume that the temperature difference $T_H - T_L$ is small. Let $E_H(x)$ be the average energy of one soliton generated at the high temperature side after it propagates over a distance x . Using Eq. (10), we can obtain

$$E_H(x) = (a_0cx + b_H)^{-1/c}, \quad (11)$$

where $b_H = (1/E_H(0))^c$. In Eq. (10), a is a constant depending on the temperature of thermal field. Here, the temperatures over the lattice may be approximated by $T_0 = (T_H + T_L)/2$ since $T_H - T_L$ is small. So, we used a_0 which is the value of a for T_0 . At the low temperature side, the average energy carried by one soliton is given by $E_H(N)$.

Let $\sigma(T_H)$ be the average number of solitons generated at high temperature side per unit time. The energy J_H transported by solitons from the high temperature side to the low temperature one per unit time may be given by

$$J_H = \sigma(T_H) \cdot E_H(N) \quad (12)$$

For $N \gg 1$, J_H is approximated by

$$J_H \approx \sigma(T_H) \cdot (a_0 c N)^{-1/c} \quad (13)$$

from Eq.(11). Similarly, the energy flux J_L of soliton in the opposite direction is obtained as $J_L \approx \sigma(T_L) \times (acN)^{-1/c}$. The net energy flux J_s via the soliton channel is obtained for $N \gg 1$ as follows:

$$J_s = J_H - J_L \approx \{\sigma(T_H) - \sigma(T_L)\} (a_0 c N)^{-1/c}. \quad (14)$$

This indicates the scaling law $J_s \propto N^{-1/c}$, where $0 < 1/c < 1$ holds from our numerical results. Since the energy flux J_{ph} via the phonon channel was assumed to follow $J_{ph} \propto N^{-1}$, the soliton energy flux J_s is dominant when $N \gg 1$ compared with J_{ph} . Therefore, the total energy flux J is approximately given by $J \approx J_s$, and we have

$$J \approx J_s \propto N^{-1/c}. \quad (15)$$

The thermal conductivity κ is defined by

$$\kappa = \frac{J}{(T_H - T_L)/N}. \quad (16)$$

Combining Eqs. (15) and (16), we arrive at the scaling law

$$\kappa \propto N^{1-1/c}. \quad (17)$$

Recall that the anomalous heat transport in the FPUT- β lattice is characterized by $\kappa \propto N^\alpha$ with $0 < \alpha < 1$. Equation (17) shows that the present theory can reproduce a scaling law of the same form. Moreover, the exponent is given by $\alpha = 1 - 1/c$. If we calculate α by using $c \approx 1.65$ which was obtained by our numerical experiments, we have $\alpha \approx 0.394$. This value of α is in good agreement with the value $\alpha \approx 0.3987$ of a direct nonequilibrium simulation [10]. This fact indicates that the energy transport by attenuating soliton is a promising candidate for the mechanism of anomalous heat transport.

Acknowledgments

This work was supported by a Grant-in-Aid for Scientific Research (C), No. 22K03451 from Japan Society for the Promotion of Science (JSPS).

References

- [1] C. W. Chang *et al.*, "Breakdown of Fourier's Law in Nanotube Thermal Conductors," *Phys. Rev. Lett.*, vol. 101, 075903, 2008.
- [2] G. Casati *et al.*, "One-Dimensional Classical Many-Body System Having a Normal Thermal Conductivity," *Phys. Rev. Lett.*, vol. 52, pp. 1861–1864, 1984.
- [3] T. Prosen and M. Robnik, "Energy transport and detailed verification of Fourier heat law in a chain of colliding harmonic oscillators," *J. Phys. A*, vol. 25, pp. 3449–3472, 1992.
- [4] K. Aoki and D. Kusnezov, "Bulk properties of anharmonic chains in strong thermal gradients: non-equilibrium φ^4 theory," *Phys. Lett. A*, vol. 265, pp. 250–256, 2000.
- [5] M. Toda, "Solitons and Heat Conduction," *Physica Scripta*, vol. 20, pp. 424–430, 1979.
- [6] K. Yoshimura, Y. Doi, and T. Kitamura, "Heat transport in nonlinear lattices free from the umklapp process," *Phys. Rev. E*, vol. 105, 024140, 2022.
- [7] S. Lepri, R. Livi, and A. Politi, "Heat Conduction in Chains of Nonlinear Oscillators," *Phys. Rev. Lett.*, vol. 78, pp. 1896–1899 (1997).
- [8] L. Wang and T. Wang, "Power-law divergent heat conductivity in one-dimensional momentum-conserving nonlinear lattices," *Europhys. Lett.*, vol. 93, 54002, 2011.
- [9] G. Dematteis *et al.*, "Coexistence of Ballistic and Fourier Regimes in the β Fermi-Pasta-Ulam-Tsingou Lattice," *Phys. Rev. Lett.*, vol. 125, 024101, 2020.
- [10] M. Takatsu, T. Kitamura, and K. Yoshimura, "A Large Scale Non-equilibrium Simulation of Heat Transport in One-dimensional Fermi-Pasta-Ulam-Tsingou Lattice," *J. Phys. Soc. Jpn.*, vol. 93, 053001, 2024.
- [11] S. Lepri, "Memory effects and heat transport in one-dimensional insulators," *European Physical Journal B*, vol. 18, pp. 441–446, 2000.
- [12] T. Hatano, "Heat conduction in the diatomic Toda lattice revisited," *Phys. Rev. E*, vol. 59, pp. R1–4, 1999.
- [13] N. Li, B. Li, and S. Flach, "Energy Carriers in the Fermi-Pasta-Ulam β Lattice: Solitons or Phonons?," *Phys. Rev. Lett.*, vol. 105, 054102, 2010.
- [14] Y. Ming *et al.*, "Solitons as candidates for energy carriers in Fermi-Pasta-Ulam lattices," *Phys. Rev. E*, vol. 97, 012221, 2018.

Space-time modulation of a nonlinear system

Juan F.R. Archilla[†], Masayuki Kimura[‡], Yusuke Doi^{*}, Víctor J. Sánchez-Morcillo[§]

[†] Group of Nonlinear Physics, Department of Applied Physics I

Universidad de Sevilla, ETSII, Avda Reina Mercedes s/n, 41012-Sevilla, Spain

[‡] Department of Electrical and Electronic Engineering, Faculty of Science and Engineering

Setsunan University, 17-8 Ikeda-Nakamachi, Neyagawa, Osaka 572-8508, Japan

^{*} Laboratory of Microdynamics, Department of Mechanical Engineering, Graduate School of Engineering

Osaka University 2-1 Yamadaoka, Suita, Osaka 565-0871, Japan

[§] IGIC, Universitat Politècnica de València, Paranimf 1, 46730 Grao de Gandia, Spain

Email: archilla@us.es, masayuki.kimura@setsunan.ac.jp, doi@mech.eng.osaka-u.ac.jp, victorsm@fis.upv.es

Abstract—We consider a model that can be modulated in time and space and can be reproduced physically as a cantilever array. We explore the linear spectrum and show that localized nonlinear excitations, as breathers, can be obtained in such a complex system.

Model and results

Dynamic metamaterials, are artificial structures that incorporate non only space modulation, but also time modulation, or space-time modulation. The modulation can be achieved with acoustic waves, voltage waves, or electromagnetic waves, that may change media parameters as permittivity, magnetic permeability, refractive index, or other properties [1].


One of the authors constructed a physical model for cantilever arrays with an on-site potential provided by electromagnets, which is therefore both nonlinear and tunable by changing the electric current [2] described by the dynamical equation:


$$\ddot{u}_n = -(\omega_0^2 - \delta \cos(hn - \Omega t))u_n + \kappa(u_{n+1} + u_{n-1} - 2u_n), \quad (1)$$

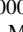
The modulation in time and space produce a transformation of the the phonon bands in $\omega - q$ space where new bands and forbidden bands appear. We develop the spectral theory [3] for the modulated systems and were able to obtain the equations of the bands (see Fig. 1):

$$\omega = +m\Omega + \sqrt{\omega_0^2 + 2\kappa(1 - \cos(q + mh))} \quad (2)$$

A modification of the system introduces nonlinearity and we are able to find breathers, both site centered and bond centered. The properties of those breathers and analyzed and related with the band spectrum.

ORCID iDs JFR Archilla:  0000-0001-6583-6114,

M Kimura:  0000-0002-1445-6266,

Y Doi:  0000-0003-3749-5353,

VJ Sánchez-Morcillo:  0000-0003-4766-1263



This work is licensed under a Creative Commons Attribution Non Commercial, No Derivatives 4.0 License. ©IEICE 2025

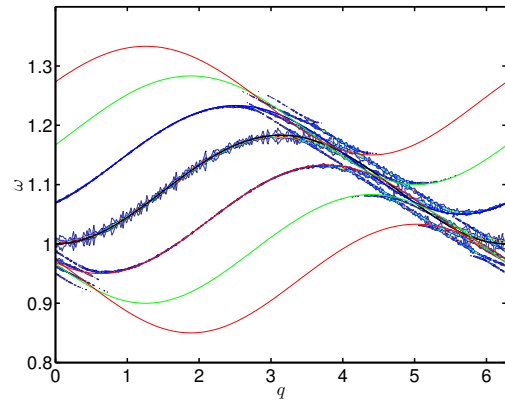


Figure 1: Theoretical and numerical frequency-momenta representation

In conclusion, modulated systems offer an striking change in the phonon spectrum providing for new nonlinear excitations to appear. As they can be engineered, they allow for the design of breather properties.

Acknowledgments

JFRA thanks project MICIU PID2022-138321NB-C22, MK acknowledges support from JSPS Kakenhi (C) No. 24K07393, YD acknowledges JSPS Kakenhi No. (C) No. 24K14978, VJSM also acknowledges MICIU PID2022-138321NB-C22.

References

- [1] C. Caloz, Z.L. Deck-Léger, A. Bahrami, O.C. Vicente, Z. Li, IEEE Antenn. Propag. M. **65**, 50 (2023)
- [2] M. Kimura, T. Hikihara, Phys. Lett. A **373**, 1257 (2009)
- [3] J.F.R. Archilla, Y. Doi, M. Kimura, Phys. Rev. E **100**(2), 022206 (2019)

Dispersive shock waves from discrete to continuum: some vignettes

P.G. Kevrekidis^{†,‡}

[†] Department of Mathematics & Statistics
University of Massachusetts, Amherst, MA 01003, USA

[‡] Department of Physics
University of Massachusetts, Amherst, MA 01003, USA
Email: kevrekid@umass.edu

Abstract—In this talk we will seek to present some case examples of the study of Dispersive Shock Waves (DSWs) in discrete systems. Our motivation will stem from experiments in granular crystals and related systems. In the presence of precompression, connections with Fermi-Pasta-Ulam-Tsingou (FPUT) type lattices and both the Korteweg-de Vries continuum, as well as the Toda discrete integrable limits will be leveraged to analyze the dynamics. In the absence of precompression (highly nonlinear case), a dispersionless continuum approach will yield information regarding the breakup time. To obtain further details regarding the DSWs, we will embark in a quasi-continuum formulation, analyzing its traveling waves, periodic solutions, conservation laws, and Whitham modulation equations. Our findings are compared with simulations of the quasi-continuum model and of the original discrete lattice, both at the level of a bi-directional quasi-continuum model and for a unidirectional variant. Time permitting, a discrete variant of the Burgers' equation will also be considered to provide a palette of phenomenologies featuring similarities and differences in comparison to the continuum Burgers' model.

These vignettes are part of a broader effort and attempt to explore the impact of Riemann-type initial conditions in nonlinear dynamical lattices. Time permitting, we will hopefully showcase that such intriguing features and rich phenomenologies are not particular to the FPUT system, but can also arise in discrete variants of the nonlinear Schrödinger equation. Additionally, should the opportunity arise, we intend to showcase the application of data-driven methods and conclusions they can give rise to in such complex, nonlinear, lattice dynamical systems.

Acknowledgments

This material is based upon work supported by the U.S. National Science Foundation under the awards PHY-2110030, PHY-2408988 and DMS-2204702 (PGK).

ORCID iDs P.G. Kevrekidis 0000-0002-7714-3689



: This work is licensed under a Creative Commons Attribution Non Commercial, No Derivatives 4.0 License. ©IEICE 2025

Effect of Impurity Distribution on Propagation Speed of Nonlinear Localized Oscillation in a Mass-Spring Chain

Yosuke Watanabe[†] and Yusuke Doi[‡]

[†] Department of Mechanical Engineering, Faculty of Science and Engineering, Setsunan University
17-8 Ikedanaka-machi, Neyagawa, Osaka 572-8508, Japan

[‡] Department of Adaptive Machine Systems, Graduate School of Engineering, Osaka University
2-1 Yamadaoka, Suita, Osaka 565-0871, Japan

Email: yosuke.watanabe@setsunan.ac.jp, doi@mech.eng.osaka-u.ac.jp

Abstract– Propagation of nonlinear localized oscillation in a mass-spring chain with impurities is studied experimentally and numerically. Letting the mass at one end of the chain driven sinusoidally at high frequency and large amplitude, localized oscillations can be excited intermittently near the end and propagated down the chain one after another at a constant speed. We study the effect of the distribution of impurities in the chain on the propagation of localized oscillations.

1. Introduction

It is known that, letting the oscillator at one end of the chain driven sinusoidally at high frequency and large amplitude, robust localized oscillations (intrinsic localized modes (ILMs) or discrete breathers (DBs) [1, 2]) can be excited intermittently near the end and propagated down the chain one after another. This phenomenon is interesting from the viewpoint of energy propagation in discrete periodic systems and is called supratransmission [3, 4]. We have experimentally observed the supratransmission by a mechanical mass-spring chain which emulates the Fermi-Pasta-Ulam (FPU) one of beta type [5]. At one end of the chain the device to drive the end sinusoidally in the direction of the array is attached and at the other end the chain is simply fixed. Keeping driving the end at a high frequency, we can observe that the localized oscillations excited at intervals propagate down the chain one after another and are reflected at the fixed end. Our experimental results show that there are the thresholds about the driving amplitude and frequency where no localized oscillations are excited. Our experiments also show that the propagation speed remains almost constant throughout its propagation. On the contrary, the speed could be changed, if there are some impurities or distribution of impurities in the chain.

2. Experimental Results

The impurities may be given by replace some oscillators with different weight ones or by addition of on-site effects at some oscillators. In our previous studies in which some consecutive oscillators in the chain were replaced by heavier ones, we observed slowdown of the propagation at the impurity section [6] (Fig. 1). Appropriate arrangements of impurities will be effective to control the propagation. In parallel with the experiments, we are carrying out numerical calculations for the analytical model. Both of the results should be compared.

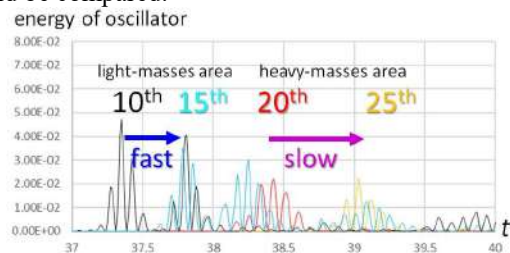


Fig. 1. Slowdown of the propagation of ILM in the heavy-masses area in the chain.

References

- [1] A. J. Sievers and S. Takeno, "Intrinsic localized modes in anharmonic crystals," *Phys. Rev. Lett.*, vol. 61 (8), pp. 970-973, 1988.
- [2] D. K. Campbell, S. Flach and Y. S. Kivshar, "Localizing energy through nonlinearity and discreteness," *Phys. Today*, vol. 57, pp. 43-49, 2004.
- [3] F. Geniet and J. Leon, "Energy transmission in the forbidden band gap of a nonlinear chain," *Phys. Rev. Lett.*, vol. 89 (13), 134102, 2002.
- [4] R. Khomeriki, S. Lepri and S. Ruffo, "Nonlinear supratransmission and bistability in the Fermi-Pasta-Ulam model," *Phys. Rev. E*, vol. 70, 066626, 2004.
- [5] Y. Watanabe, T. Nishida, Y. Doi and N. Sugimoto, "Experimental demonstration of excitation and propagation of intrinsic localized modes in a mass-spring chain," *Phys. Lett. A*, vol. 382, pp. 1957-1961, 2018.
- [6] Y. Watanabe and Y. Doi, "Experimental and Numerical Study on Propagation of Nonlinear Localized Oscillation in a Mass-Spring Chain with Impurities," *Proc. NOLTA2024*, p. 228, 2024.

ORCID iDs First Author: 0000-0002-7289-2787, Second Author: 0000-0003-3749-5353



This work is licensed under a Creative Commons Attribution Non Commercial, No Derivatives 4.0 License. ©IEICE 2025

Velocity of the traveling intrinsic localized mode in the real self-dual nonlinear network lattice

Masayuki Sato and Yukihiro Soga[†]

[†]School of Mathematics and Physics, Kanazawa University
Kakumamachi, Kanazawa, 920-1192, Japan,

Email: msato153@staff.kanazawa-u.ac.jp, ysoga@staff.kanazawa-u.ac.jp

Abstract– In the self-dual nonlinear network lattice, the intrinsic localized mode (ILM) travels almost freely because of very small interaction with linear phonon modes even if the nonlinear lattice is not integrable. In experiments, traveling ILMs in the ring-shaped lattice can be maintained by using a propagating wave driver that is necessary to compensate for the energy loss due to damping. Amplitude and velocity increases with the driver frequency, because of the positive nonlinearity of the lattice. Small steps are observed in velocity curve when plotted it as a function of the driver frequency. Between adjacent steps, (velocity)/(driver frequency) is kept about a constant and this implies synchronization between rotational motion of the ILM in the ring and ILM vibration takes place. Simulations reveal that larger damping at zero voltage (and current) is important for the appearance of steps.

1. Introduction

Nonlinear electric networks have been studied for generating high power and high frequency signals.[1, 2, 3] Capacitors and inductors are used for composing the lattices. When those capacitors and inductors are balanced with each other, that is, both have the same nonlinear functionality on voltage or current, the lattice equations become self-dual.[4, 5] In the self dual nonlinear network lattice, the Intrinsic localized modes (ILMs) can travel smoothly because of almost no interaction with the linear phonon modes, even if the lattice is not integrable.[6, 7] In a real experimental lattice, a driver is necessary to keep the ILM amplitude at a steady condition to compensate an energy loss due to damping. At such case, the driver frequency can be a good controlling parameter, and traveling velocity is an observable value which is sensitive to change of the ILM condition in the lattice. By measuring traveling velocity as a function of the driver frequency, we could study about the interaction between the traveling ILM and the linear phonon modes. [8]

In this paper, we report about the ILM velocity in the

self dual network lattice as a function of the driver frequency, which shows steps that is related to a synchronization between the ILM traveling in the ring shaped lattice and ILM vibration. ILM velocity is almost proportional to the driver frequency, however, there should be a boosting mechanism of the ILM that makes ILM faster than usual. Otherwise, the ILM was kept at around one synchronized state and no steps were appeared. This boosting mechanism may be related to the large damping at $V=0$, which is different from a fixed resistors model.

2. Experiments

Lattice is composed from 32 elements connected to the ring shape. To generate the traveling ILM experimentally, we used the traveling wave driver which is expressed as



$$V_{d,n} = V_d \cos(k_d n - \Omega t) \quad (1)$$

where V_d is the driving amplitude, k_d is the driving wavenumber, $\Omega = 2\pi F$ is the driving frequency. By choosing k_d , then increasing the driver frequency from

the linear resonance frequency $\omega(k) = \frac{2}{\sqrt{L_{0,t} C_{0,t}}} \sin\left|\frac{k}{2}\right|$ of

the normal mode at k_d , one can generate the traveling ILM. Sometimes multi ILMs are obtained, however, one can reduce the number of the ILM to one by increasing the driver frequency up and down, or instant shorting one of the capacitor. Voltage patterns are recorded by a 32 channel oscilloscope. Velocity and the traveling pattern are measured simultaneously.

Figure 1 shows single ILM velocity as a function of the driver frequency. Numbers after letter k indicate the driver wavenumber, for example, k9 means $k_d = 9\pi/16$. For all different wavenumbers, velocity is almost proportionally increasing with the driver frequency F , with up steps. To see how the velocity changes relative to the driver frequency, v/F is plotted in Fig. 2. Here, dashed horizontal lines are at $v/F = 32/m$, where m is an integer listed right-outside of the figure nearby each line. This figure implies taking place of a synchronization between the ILM rotation in the ring and the ILM vibration, because the lines are at where the rotation time $32/v$ is integer multiple of the vibration period $1/F$. Note that at

ORCID iDs M. Sato:  0000-0003-3364-5270, Y. Soga:  0000-0001-5482-3414



This work is licensed under a Creative Commons Attribution Non Commercial, No Derivatives 4.0 License. ©IEICE 2025

higher frequencies for $k_d = 11\pi/16$, m reaches to 11 which is the same number after the letter k. At this case, $v = (32/11)F = \Omega/k_d$ indicating the localized state travels at the phase velocity so that the ILM changes into a pulse. Similarly, the pulse is observed for k9 and k10 at higher frequencies.

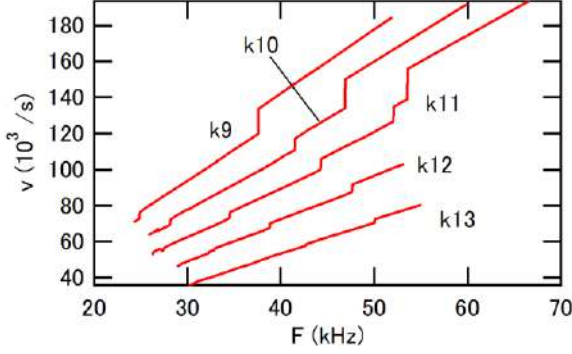


Fig. 1 Observed velocity for k9 to k13 as a function of the driver frequency. Only up sweeping results are shown. In all cases, up-steps are observed. Those are not due to resonance trapping by a linear normal mode that causes down steps in the velocity.[8]

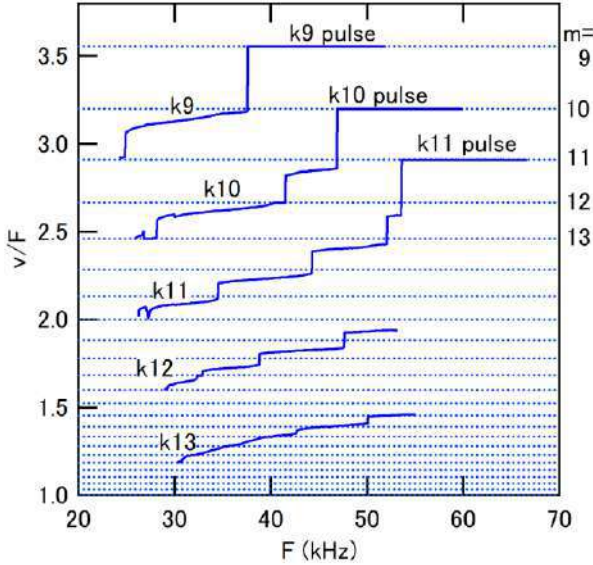


Fig. 2 Velocity divided by driver frequency F . Horizontal dashed lines are at $32/m$, where m is an integer. $v/F = 32/m$ is from multiple of one cycle vibration, m/F , equals to the single rotation time, $32/v$. This figure indicates that the velocity is affected by a synchronization phenomenon between the vibration and lateral rotation. The integer number m at right side of the figure indicate corresponding number of nearest dashed horizontal line. Since the pulse travels at the phase velocity $v = 2\pi F / k_d$, Integer $m=9$ for k9 driver means the pulse because $v = 2\pi F / (9\pi/16) = 32F/9$.

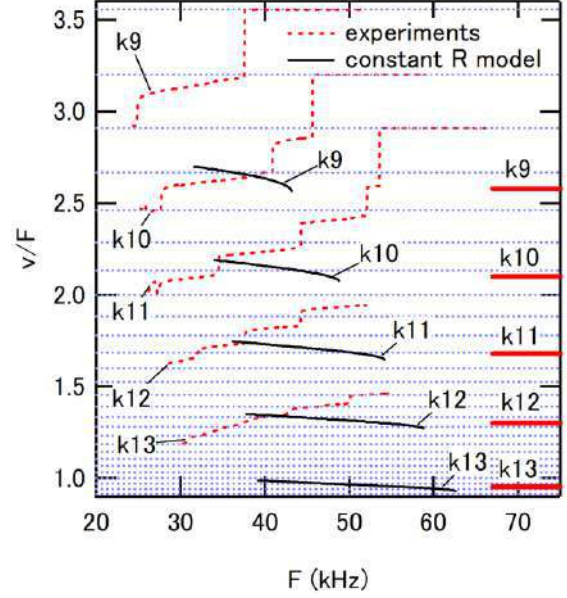


Fig. 3 Comparison of the experiments and the simple constant-R model simulations by Eqs. (2)-(3). Dashed curves are from experiments, and solid curves are by the constant-R simulations. Thick horizontal lines are calculated from the nonlinear group velocity, considering the bandwidth widening, $v_g / F = \pi / \tan[k_d / 2]$. As showing in this figure, velocity of the constant-R model is well estimated by the nonlinear group velocity. In addition, it is clear that the experimental velocity is much faster than these estimations for all different wavenumbers. Roughly, it is about 40% faster than the simple estimations.

3. Simulations

We have performed simulations using following equations of motions

$$\left(\frac{C_0}{\sqrt{1+V_n^2/V_0^2}} + C_d \right) \frac{dV_n}{dt} = I_{n-1} - I_n - \frac{V_n}{R_p} + C_d \frac{dV_{d,n}}{dt} \quad (2)$$

$$\left(\frac{L_0}{\sqrt{1+I_n^2/I_0^2}} + L_{adj} \right) \frac{dI_n}{dt} = V_n - V_{n+1} - I_n R_L \quad (3),$$

$$+ M_d \frac{dI_{d,n+0.5}}{dt}$$

where $C_0 = 117nF$, $V_0 = 4.24V$, $C_d = 10nF$ are parameters for the nonlinear capacitor (TMK107F104ZZ-T Taiyo-Yuden), and $L_0 = 1.0mH$, $I_0 = 0.0459A$, $L_{adj} = 85.5\mu H$ are parameters for the nonlinear inductor, that is composed from two toroidal inductors and one fixed inductor designed to match the capacitor.[7] $R_p = 776\Omega$ and $R_L = 11.0\Omega$ are parallel resistance of the capacitor and series resistance of the inductor, respectively. Driving was

made at amplitude of $V_d = 15V$ and $M_d I_d = 13.9\mu HA$ with the propagating wave driver by Eq. (1). Here, we assumed that resistances are fixed at constants. Resistances are chosen as the simulated stable ILM frequency range matches with the experimental frequency range. In experiments, there is no driver at the current equation, however, this difference doesn't relate to the velocity.

Figure 3 shows the comparison between experimental velocity and simulated one based on Eqs. (2)-(3). Simulated velocity is slower than the experimental velocity, and those are very close to the group velocity at each wave-number indicated by thick horizontal lines at right side of the figure. Those group velocities are calculated by taking into account the nonlinear shift of the dispersion curve,

$$\omega'(k) = \frac{2}{\sqrt{L_{0,t} C_{0,t}}} \alpha \sin\left|\frac{k}{2}\right| \quad (4)$$

where the shift parameter α is calculated by $\alpha = \frac{\Omega}{\omega(k_d)}$,

as if the dispersion curve is shifted up to the driving point $(k, \omega) = (k_d, \Omega)$. Then, the group velocity is calculated as

$$v_g = \frac{d\omega'}{dk} = \frac{1}{\sqrt{L_{0,t} C_{0,t}}} \alpha \cos\left|\frac{k}{2}\right| = \cot\left|\frac{k}{2}\right| \pi F. \quad (5)$$

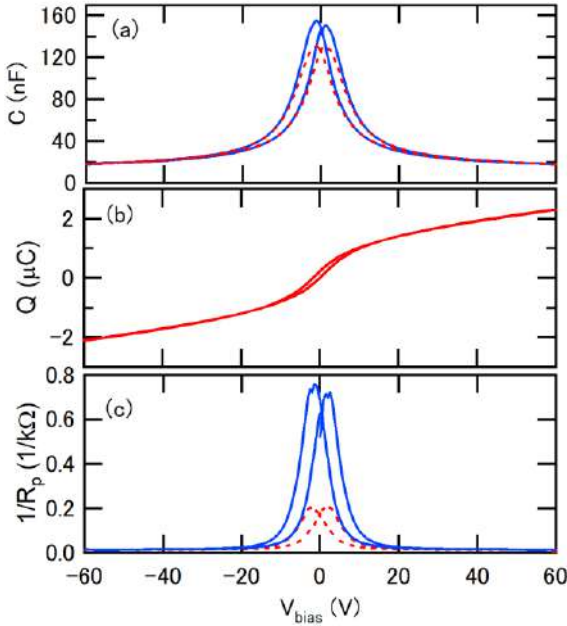


Fig. 4 DC bias dependency of (a) capacitance, (b) stored charge and (c) $1/R_p$ of the ceramic capacitor measured by a LCR meter at AC amplitudes, 20mV(dashed) and 1V (solid). The capacitor includes C_d . Stored charge is calculated from capacitance in panel (a) at 20mV AC amplitude. A small hysteresis loop is observed in panel (b). In panel (c), $1/R_p$ depends strongly on AC amplitude. In general, area of the hysteresis loop in (b) is proportional to the energy loss. As increasing the AC amplitude, area of the mini-loop becomes large.

The constant-R model by Eqs. (2)-(3) cannot explain experimental results even if we tuned parameters. One possible difference between the real lattice and the simple simulation is the damping. The damping by Eq. (2) increases with voltage. Similarly, it by Eq. (3) does with current. This dependence is very different from $1/R_p$ shown in Fig. 4. To see the effect of the large damping at $V=0$ and $I=0$, we have tested following equations.

$$\frac{dV_n}{dt} = \frac{1}{\frac{C_0}{\sqrt{1+V_n^2/V_0^2}} + C_d} \left(I_{n-1} - I_n + C_d \frac{d}{dt} V_{d,n} \right) \quad (6)$$

$$-\gamma(V_n/V_0)V_n$$

$$\frac{dI_n}{dt} = \frac{1}{\frac{I_0}{\sqrt{1+I_n^2/I_0^2}} + L_{adj}} \left(V_n - V_{n+1} + L_d \frac{d}{dt} I_{d,n+0.5} \right)$$

$$-\gamma(I_n/I_0)I_n$$

(7)

where damping changes with voltage or current as

$$\gamma(x) = \gamma_0 + \gamma_1 \frac{1}{\sqrt{1+x^2}}, \quad (8)$$

These keep Eqs. (6)-(7) are balanced. We assumed that the damping decreases with voltage (or current) as the same curve as the nonlinear function. Figure 5 shows velocity as a function of the peak damping with a fixed damping condition at 100V $\gamma(100V/V_0) = 10^4$. The velocity increases with peak of the damping at $V=0$.

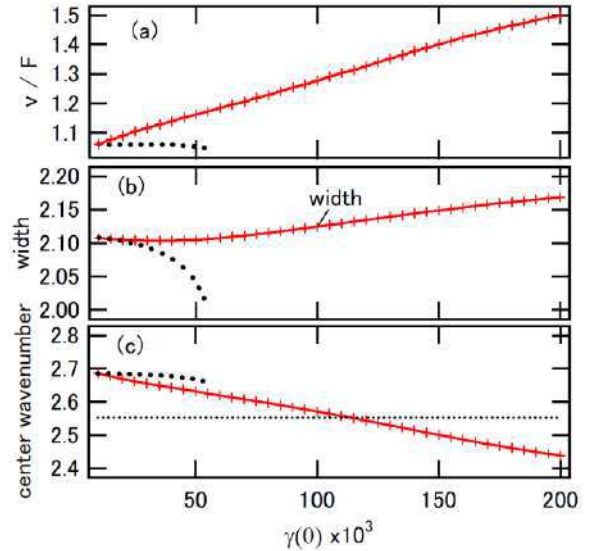


Fig. 5 Velocity enhancement by the damping at $V=0$, simulated at 50kHz driver frequency. (a) Velocity/frequency as a function of $\gamma(0)$, keeping $\gamma(100V/V_0) = 10^4$. As increasing the damping parameter $\gamma(0)$, the velocity is increasing. Dotted curves are for the constant damping model $\gamma(0) = \gamma(100)$. (b) Fitted Gaussian width of ILM

dispersion line(DL) in the k-space. (c) Fitted Gaussian center wavenumber of the ILM DL. The velocity boosting in panel (a) is due to the shift of the center wavenumber.

4. Discussions

4.1 Synchronization and steps

When the ILM changed to the pulse, velocity curves are followed perfectly to one dashed horizontal line. On the other hand, velocity between steps of the ILM in Fig. 2 look like avoiding dashed horizontal lines and stayed between them. Velocity increases gradually, and steps are observed when the velocity is reached to the dashed horizontal line. The driven-damped ILM is a stable state under a balance of energy feeding and damping. Avoiding lines can be explained as follows. The perfect synchronization makes energy feeding effectively fixed. Rather, the ILM can tune its energy feeding by slight de-synchronization when the velocity is at between those lines. The steps are observed when this tuning cannot be made at the particular range. In addition, such steps are observed because of the wide stable frequency range of the self-dual network lattice.

Synchronization between the lateral motion of the ILM (discrete breather) and ILM vibration in the discrete sine-Gordon lattice at the driven-damped lattice.[9] At that case, a synchronization plateau is observed when velocity is plotted as a function of the driving amplitude. One lattice point forwarding during two or three vibration periods are reported. So the synchronization phenomena may be a common feature of such driven-damped system.

4.2 Velocity boosting and the damping model

To appear the velocity steps like Fig. 2, ILM velocity naturally increases with the driver frequency faster than F^1 , for example, as $F^{1.5}$. The damping model by Eqs. (8)-(9) provides a possibility for explaining the faster velocity by the damping model with the peak at $V=0$. Figures 5(b)-(c) shows the dispersion line analysis of the traveling ILM, by taking 2-D Fourier transform of the voltage pattern $V_n(t)$. The transformation gives Fourier amplitude in (k, ω) space, and Fourier amplitude is observed along a line with its slope is the same to the velocity. The Fourier amplitude along the line looks Gaussian, centered at the driving point k_d . [6] Figure 5(b) shows the width of the DL amplitude, and Fig. 5(c) plots the center wavenumber of the Gaussian peak. The width is gradually increasing with the $V=0$ damping $\gamma(0)$. This may be due to a narrowing in the real space because the damping works effectively at both sides of the ILM where amplitude is smaller than the ILM center. The center wavenumber shown in Fig. 5(c) shifts lower wavenumber as increasing $\gamma(0)$. This shift causes increasing velocity because the group velocity increasing. Currently, we cannot

explain the reason of the shift. In addition, the model by Eq. (8) does not perfectly mimic the experimental devices, because the damping at $V=0$ depends on the AC vibration amplitude for the real capacitor. Thus, the damping should be a function of the maximum voltage at a half cycle of the vibration before V crosses with 0, that is $\gamma(V_{\max})$, but not a function of the instant voltage $\gamma(V)$. With the equations of motion by Eqs. (8)-(9), such damping cannot be modeled.

5. Summary

Experimental velocity of the single traveling ILM is measured in the ring shaped, 32 unit-cell self-dual nonlinear electrical network lattice. It increases with the driver frequency mostly. Step structure is clearly observed in v/F , that implies synchronization between the rotation in the ring and the vibration of the ILM affects on the velocity. Simulations based on the simple damping model reveal that the experimental velocity is faster than the simple model, which follows the group velocity calculation. The anomalous velocity boosting may be ascribed to the large damping at $V=0$ and $I=0$.

References

- [1] Hybrid Nonlinear Transmission Lines Used for RF Soliton Generation L. P. Silva Neto and J. J. Barroso, IEEE Trans. Plasma Sci. 46, 3648(2018)
- [2] A Review of Nonlinear Transmission Line System Design, IEEE Access 8, 148606(2020)
- [3] Theory and practice of pulse compression in hybrid and gyromagnetic non-linear transmission lines, M. Rahman and K. Wu, J. Appl. Phys. 132, 223902(2022)
- [4] Exact N-Soliton Solution of Nonlinear Lumped Self-Dual Network Equations, R. Hirota, J. Phys. Soc. Jpn. 35, 289 (1973)
- [5] Exact Description of the Discrete Breathers and Solitons Interaction in the Nonlinear Transmission Lines, M. M. Bogdan and D. V. Laptev, J. Phys. Soc. Jpn. 83, 064007(2014)
- [6] Propagating intrinsic localized mode in a cyclic, dissipative, self-dual one-dimensional nonlinear transmission line, M. Sato, H. Furusawa, Y. Soga and A. J. Sievers, PRE 107, 034202(2023)
- [7] Experimental study of intrinsic localized mode mobility in a cyclic, balanced, 1D nonlinear transmission line, M. Sato, H. Furusawa, M. Sakai, Y. Soga and A. J. Sievers, CHAOS 33, 073149(2023)
- [8] Experimental investigation of supertransmission for an intrinsic localized mode in a cyclic nonlinear transmission line, M. Sato, H. Furusawa, M. Sakai, Y. Soga and A. J. Sievers, CHAOS 32, 033118(2022)
- [9] Mode-locking of mobile discrete breathers, D. Zueco, P. J. Martínez, L. M. Floría, and F. Falo, Phys. Rev. E 71, 036613(2005)